

Band Structure and Fermi Surface of White Tin as Derived from de Haas-van Alphen Data*†

J. E. CRAVEN

Department of Physics, The James Franck Institute, The University of Chicago, Chicago, Illinois 60637

(Received 15 July 1968)

A semiempirical local pseudopotential model for the band structure and Fermi surface of white tin is generated using extensive de Haas-van Alphen (dHvA) extremal areas for the tin Fermi surface. The effects of spin-orbit interactions are included as a perturbation on the model Hamiltonian. Quantitative as well as qualitative agreement between the model and all aspects of the dHvA data is obtained. The quantitative agreement of the model with several other experiments is very good and is discussed in detail.

I. INTRODUCTION

THIS paper presents the results of a semiempirical local pseudopotential calculation for the band structure and Fermi surface of white tin. Metallic tin has been the subject of extensive investigations in recent years. Its availability at very high purity makes it particularly suitable for the study of general electronic properties. At around 1°K, electron mean free paths (for large-angle scattering) of approximately 1 mm in length can be obtained. A multitude of experiments, some concerned with purely dynamical properties of the electrons,¹⁻¹² others with the Fermi surface itself,¹³⁻³³ have all made contributions to the understanding of the electronic structure of this material.

Weisz³⁴ attempted to encompass much of the available experimental information with his band-structure calculation for white tin. Using a semiempirical approach, he depended primarily on the rf size-effect data of Gantmakher.^{21,22} Recent semiempirical band-structure calculations for magnesium,³⁵ zinc,³⁶ and cadmium³⁶ have shown that band structures generated using data obtained from de Haas-van Alphen (dHvA) investigations of these materials exhibit excellent quantitative as well as qualitative agreement with all experimental data. At the time of Weisz's calculation, no complete set of dHvA data was available for white tin. To provide a test of the accuracy of Weisz's model, an extensive dHvA investigation of metallic tin was made. The qualitative analysis of the results of that investigation in terms of Weisz's Fermi-surface model was presented in Ref. 13. The analysis showed that Weisz's model was qualitatively correct, but that quantitatively the agreement between the calculated extremal areas and those measured by experiment was poor.

The quantitative inadequacy of Weisz's model necessitates a redetermination of the band structure and Fermi surface of white tin taking full advantage

* Supported in part by the National Science Foundation and the Advanced Research Projects Agency.

† Submitted in partial fulfillment of the requirements for the degree of Doctor of Philosophy at the University of Chicago.

¹ A. R. Mackintosh, *Phys. Rev.* **131**, 2420 (1963).

² J. R. Leibowitz, *Phys. Rev.* **133**, A84 (1964).

³ V. N. Kachinskii, *Zh. Eksperim. i Teor. Fiz.* **43**, 1158 (1962) [English transl.: *Soviet Phys.—JETP* **16**, 818 (1963)].

⁴ D. A. Hays and W. L. McLean, *Phys. Rev.* **168**, 755 (1968).

⁵ B. N. Aleksandrov, *Zh. Eksperim. i Teor. Fiz.* **43**, 399 (1962) [English transl.: *Soviet Phys.—JETP* **16**, 286 (1963)].

⁶ B. N. Aleksandrov, *Zh. Eksperim. i Teor. Fiz.* **43**, 1231 (1962) [English transl.: *Soviet Phys.—JETP* **16**, 871 (1963)].

⁷ R. C. Young, *Phys. Rev. Letters* **15**, 262 (1965).

⁸ R. C. Young, *Phys. Rev.* **152**, 659 (1966).

⁹ V. F. Gantmakher and Yu. V. Sharvin, *Zh. Eksperim. i Teor. Fiz.* **48**, 1077 (1965) [English transl.: *Soviet Phys.—JETP* **21**, 720 (1965)].

¹⁰ V. B. Zernov and Yu. V. Sharvin, *Zh. Eksperim. i Teor. Fiz.* **36**, 1038 (1959) [English transl.: *Soviet Phys.—JETP* **9**, 737 (1959)].

¹¹ Yu. V. Sharvin and V. F. Gantmakher, *Zh. Eksperim. i Teor. Fiz.* **38**, 1456 (1960) [English transl.: *Soviet Phys.—JETP* **11**, 1062 (1960)].

¹² V. F. Gantmakher and Yu. V. Sharvin, *Zh. Eksperim. i Teor. Fiz.* **39**, 1242 (1960) [English transl.: *Soviet Phys.—JETP* **12**, 358 (1961)].

¹³ J. E. Craven and R. W. Stark, *Phys. Rev.* **168**, 849 (1968).

¹⁴ M. D. Stafleu and A. R. DeVroomen, *Phys. Letters* **23**, 179 (1966).

¹⁵ M. D. Stafleu and A. R. DeVroomen, *Phys. Status Solidi* **23**, 675 (1967).

¹⁶ J. G. Anderson and R. C. Young, *Phys. Rev.* **168**, 696 (1968).

¹⁷ A. V. Gold and M. G. Priestley, *Phil. Mag.* **5**, 1089 (1960).

¹⁸ N. E. Alekseevskii, Yu. P. Gaidukov, I. M. Lifshitz, and V. G. Peschanskii, *Zh. Eksperim. i Teor. Fiz.* **39**, 1201 (1960) [English transl.: *Soviet Phys.—JETP* **12**, 837 (1961)].

¹⁹ N. E. Alekseevskii and Yu. P. Gaidukov, *Zh. Eksperim. i Teor. Fiz.* **41**, 1079 (1961) [English transl.: *Soviet Phys.—JETP* **12**, 770 (1962)].

²⁰ M. S. Khaikin, *Zh. Eksperim. i Teor. Fiz.* **43**, 59 (1962) [English transl.: *Soviet Phys.—JETP* **16**, 42 (1963)].

²¹ V. F. Gantmakher, *Zh. Eksperim. i Teor. Fiz.* **44**, 811 (1963) [English transl.: *Soviet Phys.—JETP* **17**, 549 (1963)].

²² V. F. Gantmakher, *Zh. Eksperim. i Teor. Fiz.* **46**, 2028 (1964) [English transl.: *Soviet Phys.—JETP* **19**, 1366 (1964)].

²³ V. F. Gantmakher and E. A. Kaner, *Zh. Eksperim. i Teor. Fiz.* **45**, 1430 (1963) [English transl.: *Soviet Phys.—JETP* **18**, 988 (1964)].

²⁴ M. S. Khaikin, *Zh. Eksperim. i Teor. Fiz.* **42**, 27 (1962) [English transl.: *Soviet Phys.—JETP* **15**, 18 (1963)].

²⁵ M. S. Khaikin, *Zh. Eksperim. i Teor. Fiz.* **43**, 59 (1962) [English transl.: *Soviet Phys.—JETP* **16**, 42 (1963)].

²⁶ J. F. Koch and A. F. Kip, *Phys. Rev. Letters* **8**, 473 (1962).

²⁷ M. S. Khaikin, *Zh. Eksperim. i Teor. Fiz.* **39**, 513 (1960) [English transl.: *Soviet Phys.—JETP* **12**, 359 (1961)].

²⁸ A. A. Galkin, E. A. Kaner, and A. P. Korolyuk, *Zh. Eksperim. i Teor. Fiz.* **39**, 1517 (1960) [English transl.: *Soviet Phys.—JETP* **12**, 1055 (1961)].

²⁹ T. Olsen, *J. Phys. Chem. Solids* **24**, 649 (1963).

³⁰ R. J. Kearney, A. R. Mackintosh, and R. C. Young, *Phys. Rev.* **140**, A1671 (1965).

³¹ B. I. Miller, *Phys. Rev.* **151**, 519 (1966).

³² E. Fawcett, *Proc. Roy. Soc. (London)* **A232**, 519 (1955).

³³ R. G. Chambers, *Can. J. Phys.* **34**, 1395 (1956).

³⁴ G. Weisz, *Phys. Rev.* **149**, 504 (1966).

³⁵ J. C. Kimball, R. W. Stark, and F. M. Mueller, *Phys. Rev.* **162**, 600 (1967).

³⁶ R. W. Stark and L. M. Falicov, *Phys. Rev. Letters* **19**, 795 (1967).

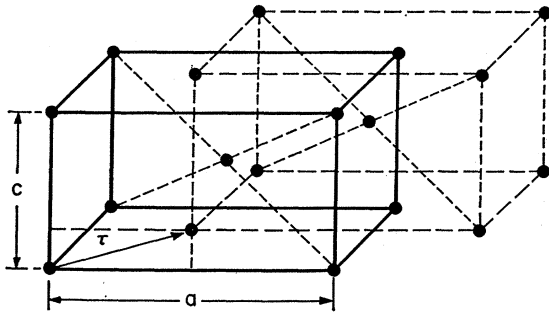


FIG. 1. Crystal lattice of white tin.

of the dHvA data. Here we present the new band structure and Fermi surface based on pseudopotential theory and utilizing the data of Ref. 13. The quantitative consistency of this new model with previous experimental data is demonstrated in Sec. VII.

II. CRYSTAL STRUCTURE

White tin crystallizes in the body-centered tetragonal lattice structure with a basis of two atoms per lattice site as shown in Fig. 1. The Brillouin zone for this structure is shown in Fig. 2. The twofold symmetric ΓL and ΓX lines are along $[100]$ and $[110]$, respectively; the fourfold symmetric ΓH line lies along $[001]$. The lattice parameters were determined from the Grüneisen rule to be $a=5.80 \text{ \AA}$, $c=3.15 \text{ \AA}$ at liquid-helium temperatures. Basis vectors for the direct and reciprocal lattices along with the atom sites in the primitive cell are given in Table I. Atomic units are used throughout this paper and energies are expressed in rydbergs.

III. FERMI-SURFACE MODEL

The present calculation yields a Fermi-surface model which has only slight qualitative differences from Weisz's while both differ substantially from the single-orthogonalized-plane-wave (OPW) model.

The single-OPW model has a hole pocket located at W in the second band. In this calculation, the first two bands are completely filled. The third band of the

single OPW model contains hole surfaces in the shape of pillars oriented along the XP zone line and multiply connected by a set of tubes joined near W . In our model the tubes are eliminated and the pillars remain in the form of closed, dumbbell-shaped hole surfaces centered at X with twofold axes of rotation along XP , XL , and XT . This sheet of our model is shown in Fig. 3(a).

The fourth band of the single-OPW model consists of two separate sheets: a closed electron sheet resembling a pair of intersecting convex lenses centered at Γ and a larger open hole surface, again centered at Γ , consisting of intersecting, elongated tubes whose principal axes are along ΓX . In our model, the two sheets retain their general shape but are found to be connected near W by a small "neck" of electrons centered on ΓH . In this way, one continuous, though reentrant, sheet is obtained with the crossed-lens electron surface located within the crossed-tube hole sheet and oriented with the lens edge along ΓX . These two aspects of our fourth-band sheet are shown in Figs. 3(b) and 3(c).

The fifth zone of the single-OPW model consists of pear-shaped electron pieces centered at H with alternately top-up and top-down orientation and multiply connected by a series of tilted tubes centered at V . Our model, shown in Fig. 3(d), retains all the qualitative features of this surface. Also found in the fifth zone of the single-OPW model is a cigar-shaped electron surface centered at Γ and oriented along ΓH . This sheet is eliminated in our model.

In the sixth band, the single-OPW model has closed, cigar-shaped electron surfaces located at V , and four similarly shaped pieces symmetrically placed near W . In our calculation the electrons at V are eliminated and those near W are merged to form a closed, rounded tooth-shaped piece centered on the ΓH line. This sheet of our model is shown in Fig. 3(e). It is in this sixth-zone sheet that we find the only noticeable qualitative divergence from Weisz's model. He also has a closed electron surface oriented on ΓH near W , but his sheet contains elongated arms extending outward beyond the HP zone line. In our calculation these arms are

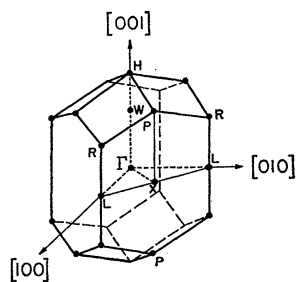


FIG. 2. First Brillouin zone for white tin. The crystallographic $[100]$, $[001]$, and $[110]$ axes are parallel to the ΓL , ΓH , and ΓX zone lines, respectively.

TABLE I. Basis vectors for the real and reciprocal lattices and atom sites in the primitive cell.

Basis vectors for real lattice	
$\mathbf{a}_1 = (\frac{1}{2}a, -\frac{1}{2}a, \frac{1}{2}c)$	
$\mathbf{a}_2 = (\frac{1}{2}a, \frac{1}{2}a, \frac{1}{2}c)$	
$\mathbf{a}_3 = (0, 0, c)$	
Basis vectors for reciprocal lattice	
$\mathbf{b}_1 = (2\pi/a, -2\pi/a, 0)$	
$\mathbf{b}_2 = (2\pi/a, 2\pi/a, 0)$	
$\mathbf{b}_3 = (-2\pi/a, 0, c)$	
Atom sites in the primitive cell	
$\tau_1 = (0, -\frac{1}{4}a, -\frac{1}{8}c)$	
$\tau_2 = (0, \frac{1}{4}a, \frac{1}{8}c)$	

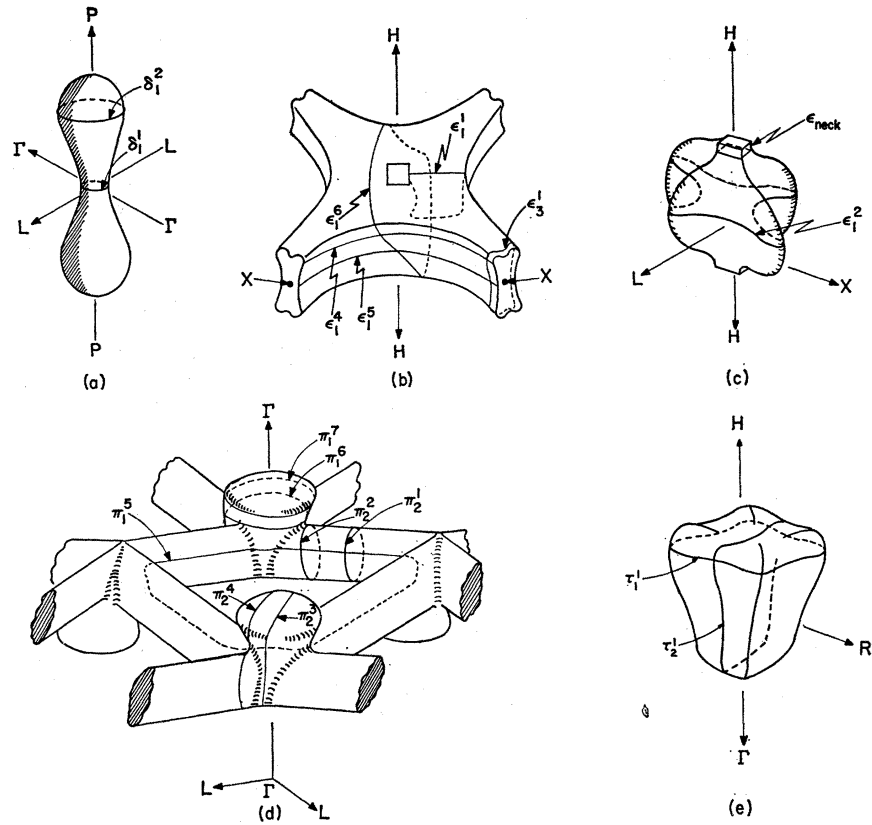


FIG. 3. Various sheets of the Fermi surface from the present calculation. Orbits corresponding to extremal cross sections on each sheet are also shown.

eliminated and only a vestigial bump is found. Weisz's sixth-zone sheet also possesses a rather pronounced waist about the closed surface in a plane perpendicular to [001]. In our calculation the waist is eliminated by the shrinking of the lower portion of the surface.

IV. dHvA EFFECT

At low temperatures, there is a sharp cutoff in the electron distribution at the Fermi energy E_F . In the presence of an applied external magnetic field \mathbf{H} , the magnetic flux enclosed within an electron orbit in the metal is quantized in units of hc/e . As the magnitude of \mathbf{H} is increased, quanta of flux are periodically expelled from the orbits associated with electron states lying nearest in energy to E_F . These periodic oscillatory changes are observable in the magnetic moment of the bulk sample which will exhibit an oscillatory field dependence of the form

$$\mathbf{M}(H, \theta, \phi, T) = \mathbf{A}_i(H, \theta, \phi, T) \sin[2\pi F_i(\theta, \phi)/H + \beta_i(\theta, \phi)], \quad (1)$$

$$\mathbf{A}_i(H, \theta, \phi, T) = \mathbf{C}_i(\theta, \phi) H^{-1/2} T [\sinh 2\pi^2 kT / \hbar \omega_0]^{-1},$$

where $\mathbf{A}_i(H, \theta, \phi, T)$ and $\beta_i(\theta, \phi)$ are the amplitude and phase of the quantum oscillations of frequency $F_i(\theta, \phi)$ for a given temperature T , field strength H , and field orientation (θ, ϕ) . $\mathbf{C}_i(\theta, \phi)$ is a vector quantity dependent upon the geometry of the Fermi surface in the im-

mediate vicinity of the extremal plane, which gives the amplitude and direction of the quantum magnetization. The frequency $F_i(\theta, \phi)$ is related to the i th extremal cross-sectional area $A_i(\theta, \phi)$ of the Fermi surface in the plane normal to \mathbf{H} by the Onsager relation³⁷

$$2\pi F_i(\theta, \phi) = (hc/e) A_i(\theta, \phi). \quad (2)$$

For a given field orientation, many frequencies can be found corresponding to extremal areas on different sheets of the Fermi surface or different extremal areas on the same sheet. From (2) we see that this, in effect, provides us with a set of extremal areas for all sheets of the Fermi surface as a function of field orientation. Figure 4 shows the dHvA spectra of extremal area branches reported in Ref. 13, and obtained using the field-modulation technique.³⁸ The notation used is that adopted in Ref. 13: The subscript denotes the crystallographic plane in which \mathbf{H} is constrained to move. The (100) plane is denoted by 1, the (001) plane is denoted by 2, and the (110) plane is denoted by 3. The superscript denotes the order of increasing size of the various extremal areas on a single sheet of the Fermi surface for the same crystallographic plane. All area branches assigned to the same sheet of the Fermi surface are designated by the same Greek letter:

³⁷ L. Onsager, Phil. Mag. 43, 1006 (1952).

³⁸ R. W. Stark and L. R. Windmiller, Cryogenics (to be published).

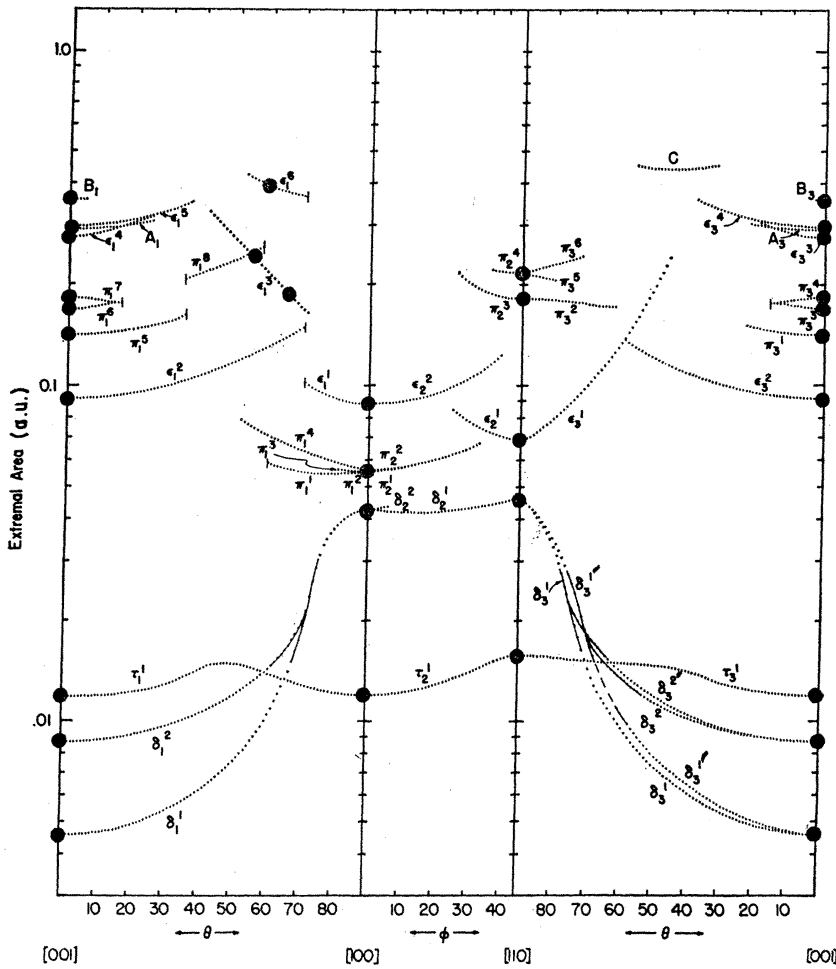


FIG. 4. dHvA extremal area branches reported in Ref. 13. The large dots are the values calculated for these branches using the local pseudopotential with the spin-orbit interaction included.

δ , ϵ , π , and τ for the third through sixth bands, respectively.

The primary problem involved in the generation of a band structure and Fermi surface using dHvA data is that of converting the dHvA area branches into \mathbf{k} vectors at the Fermi surface. Each point on a dHvA area branch can be considered an integrated, continuous set of \mathbf{k} vectors originating from some central point and terminating at the orbit on the Fermi surface. An area branch taken over a range in θ and ϕ , therefore, carries information not only about the cross sections of the Fermi surface, but of solid angles of \mathbf{k} vectors to the Fermi surface as well. The direct conversion of areas into \mathbf{k} vectors is possible only when the sheet of the surface has simply connected, closed topology with inversion symmetry.³⁹ In the more common situation where this is not the case, one must rely on area calculations based on some specific Fermi-surface model. The validity of the model is then judged by agreement between calculated and experimental areas. Since this process deals with integrated \mathbf{k} vectors rather than the \mathbf{k} vector themselves, the uniqueness of the model must

³⁹ L. L. Foldy (unpublished).

depend upon the completeness of the \mathbf{k} vector sampling taken by the dHvA data. If we describe the area branches in terms of solid angles of \mathbf{k} vectors at the Fermi surface, the dHvA data of Ref. 13 cover the entire Fermi surface. It should be noted that the one condition that immediately applies to the model is that it must obey crystal symmetry. By far the most satisfactory model representations for the Fermi surface have been those based directly on band-structure theory. These automatically satisfy the requirements of crystal symmetry and, in the process of determining the Fermi surface, yield a model for the entire band structure. Such a model determination based on pseudopotential theory is described in Sec. V.

V. PSEUDOPOTENTIAL THEORY

In the one-electron representation, the wave equation for an electron in a crystal can be written⁴⁰

$$[-\nabla^2 + V(\mathbf{r})]\psi_{\mathbf{k}} = E_{\mathbf{k}}\psi_{\mathbf{k}}, \quad (3)$$

where $V(\mathbf{r})$ is the self-consistent periodic potential of

⁴⁰ W. A. Harrison, *Pseudopotentials in the Theory of Metals* (W. A. Benjamin, Inc., New York, 1966).

the ion cores. To obtain the pseudopotential model Hamiltonian, $\psi_{\mathbf{k}}$ is generally expanded in OPW's. These functions have the property of being orthogonal to the atomiclike states within the cores while resembling plane waves in the interstitial region between cores. Thus they have the form

$$\chi_{\mathbf{k}}^{\text{OPW}} = |\mathbf{k}\rangle - \sum_{\alpha} |\alpha\rangle\langle\alpha|\mathbf{k}\rangle, \quad (4)$$

where $|\mathbf{k}\rangle$ is an ordinary plane wave and $|\alpha\rangle$ are core states of the atom. Expanded in these functions, the eigenfunction of the one-electron wave equation can be written

$$\begin{aligned} \psi_{\mathbf{k}} &= \sum_{\mathbf{g}} c_{\mathbf{k}-\mathbf{g}} \chi_{\mathbf{k}-\mathbf{g}}^{\text{OPW}} \\ &= \phi_{\mathbf{k}} - \sum_{\alpha} |\alpha\rangle\langle\alpha|\phi_{\mathbf{k}}\rangle, \\ (\phi_{\mathbf{k}} &= \sum_{\mathbf{g}} c_{\mathbf{k}-\mathbf{g}} |\mathbf{k}-\mathbf{g}\rangle), \end{aligned} \quad (5)$$

where the \mathbf{g} are reciprocal-lattice vectors and $\phi_{\mathbf{k}}$ is the pseudo wave function. Substituting this expanded form of the wave function back into the Hamiltonian and transposing the core function terms, the wave equation takes the form

$$H_p \phi_{\mathbf{k}}(\mathbf{r}) = [-\nabla^2 + V_p(\mathbf{r}, \mathbf{k})] \phi_{\mathbf{k}}(\mathbf{r}) = E_{\mathbf{k}} \phi_{\mathbf{k}}(\mathbf{r}), \quad (6a)$$

$$V_p(\mathbf{r}, \mathbf{k}) = V(\mathbf{r}) + \sum_{\alpha} (E_{\mathbf{k}} - E_{\alpha}) |\alpha\rangle\langle\alpha|. \quad (6b)$$

$V_p(\mathbf{r}, \mathbf{k})$ is the pseudopotential and E_{α} are the core eigenvalues. The pseudopotential is seen to be the sum of an attractive core potential which is strongly varying in the vicinity of each atom, and a repulsive core term involving the core functions $|\alpha\rangle$. The pseudopotential can be written as a sum of pseudopotentials associated with the individual ions;

$$V_p(\mathbf{r}, \mathbf{k}) = \sum_j U(\mathbf{r} - \mathbf{r}_j, k). \quad (7a)$$

The atomic pseudopotential depends upon the symmetry of the function upon which it operates and can, therefore, be written

$$U(\mathbf{r}, \mathbf{k}) = \sum_l U_l(\mathbf{r}, \mathbf{k}), \quad (7b)$$

where U_s operates only on functions with s symmetry, etc. In the tin atom, the lowest-energy core electrons are so tightly bound that the core is strongly localized and only the \mathbf{r} dependence is significant. The most likely source of \mathbf{k} dependence in the pseudopotential of tin is the contribution from the $4p$ and $4d$ core states. The nonlocal nature of the pseudopotential at the Fermi surface due to the contributions from these core states was found to be negligible by direct calculation of the matrix elements with $|\alpha\rangle$ and E_{α} approximated by their corresponding atomic values.⁴¹ This allows us,

⁴¹ F. Herman and S. Skillman, *Atomic Structure Calculations* (Prentice-Hall, Inc., Englewood Cliffs, N. J., 1963).

therefore, to ignore the \mathbf{k} dependence of the core terms and to approximate the pseudopotential by a purely local, or \mathbf{r} -dependent potential. A Fourier expansion of this local potential then yields

$$V_p(\mathbf{r}, \mathbf{k}) = V_p(\mathbf{r}) = \sum_{\mathbf{g}} S_{\mathbf{g}} U_{\mathbf{g}} e^{i\mathbf{g} \cdot \mathbf{r}}, \quad (8a)$$

$$S_{\mathbf{g}} = \cos(\mathbf{g} \cdot \boldsymbol{\tau}_2), \quad (8b)$$

where $S_{\mathbf{g}}$ is the structure factor, \mathbf{g} is any reciprocal-lattice vector, $\boldsymbol{\tau}_2$ is the atom site vector defined above, and the $U_{\mathbf{g}}$'s are the expansion coefficients of the Fourier series. A typical matrix element in this local approximation is then

$$\langle \mathbf{k} | H_p | \mathbf{k}' \rangle = k^2 \delta_{\mathbf{k}, \mathbf{k}'} + S_{\mathbf{g}} U_{\mathbf{g}} \delta_{\mathbf{k}-\mathbf{k}', \mathbf{g}}. \quad (9)$$

Since tin has an atomic number of 50, it is expected that its electrons experience a fairly strong effect due to spin-orbit interactions. The band structure, therefore, is subject to significant modification due to this interaction. The inclusion of spin-orbit effects in the calculation of the tin band structure and Fermi surface is, therefore, not only desirable, but necessary for an accurate representation.

The following form of the spin-orbit interaction was first suggested by Weisz:

$$H^{so}(\mathbf{k}s, \mathbf{k}'s') = \{i[\lambda_p - \lambda_d(\mathbf{k} \cdot \mathbf{k}')] \mathbf{k} \times \mathbf{k}' \cdot \boldsymbol{\sigma}_{ss'}\} \times S_{\mathbf{g}} \delta_{\mathbf{k}-\mathbf{k}', \mathbf{g}}, \quad (10)$$

where $\boldsymbol{\sigma}_{ss'}$ are the ss' components of the Pauli matrices and λ_p and λ_d are parameters reflecting the contributions of the p and d valence electron states, respectively. This expression was derived on the assumption of negligible overlap between the core orbitals and ion potentials near the atomic nuclei, and an approximation of the \mathbf{k} dependence of the OPW orthogonality coefficients. Weisz estimates these approximations good to within 1%. Because the tin atom has a $5s^2 5p^2$ valence electron configuration, the energy levels concerned with the spin-orbit interaction are expected to be mostly p -like. We, therefore, set $\lambda_d = 0$. Stark and Falicov,³⁶ in their band-structure calculations for Zn and Cd, tested the validity of this form of the spin-orbit interaction. In Cd, the strength of the spin-orbit interaction could be accurately determined from dHvA data by observing a dHvA frequency difference resulting from a spin-orbit band splitting. λ_p was then chosen so as to give the required energy splitting near the Fermi energy. That value for λ_p was found to give very good agreement between theory and experiment for all orbits which depend critically on the spin-orbit splitting of the bands. We, therefore, use this form of the spin-orbit interaction. With its inclusion in our model Hamiltonian formalism, a typical matrix element has the form

$$\begin{aligned} \langle \mathbf{k}s | H_p + H^{so} | \mathbf{k}'s' \rangle &= k^2 \delta_{\mathbf{k}, \mathbf{k}'} \delta_{ss'} \\ &+ [U_{\mathbf{g}} \delta_{ss'} + i\lambda_p \mathbf{k} \times \mathbf{k}' \cdot \boldsymbol{\sigma}_{ss'}] S_{\mathbf{g}} \delta_{\mathbf{k}-\mathbf{k}', \mathbf{g}}. \end{aligned} \quad (11)$$

TABLE II. Region symmetry points and corresponding expansion set sizes.

Symmetry pt.	No. of plane waves
H	22
V	22
R	22
$\frac{1}{2}LR$	22
L	22
$\frac{1}{2}\Gamma L$	19
Γ	21
$\frac{1}{2}\Gamma X$	22
X	20
$\frac{1}{2}XP$	22
P	20
$\frac{1}{2}\Gamma W$	17

In the semiempirical approach which we employ, the Fourier coefficients of the expanded local potential, the $U_{\mathbf{g}}$'s, are treated as variable parameters. Since there is no accurate experimental determination for the strength of the spin-orbit interaction in white tin, λ_p was also treated as a variable parameter. Those $U_{\mathbf{g}}$ with nonvanishing $S_{\mathbf{g}}$ corresponding to $|\mathbf{g}| < 2k_F$ give first-order perturbation corrections on the Fermi surface. Those $U_{\mathbf{g}}$ for which $|\mathbf{g}| > 2k_F$ give second-order perturbation effects on the Fermi surface. For white tin, four expansion coefficients with corresponding nonvanishing structure factors were found to be of first-order significance. These correspond to reciprocal lattice vector sets $[200]$, $[101]$, $[220]$, and $[211]$. To determine these coefficients and λ_p using the dHvA data of Ref. 13, the following procedure was followed:

(a) Nine experimental extremal areas were selected as representative of all sheets of the Fermi surface. At least one extremal area was chosen on each of the major sheets of the Fermi surface in each Brillouin zone so that a good representation of the entire band structure near the Fermi energy was obtained.

(b) For each area, two or more points \mathbf{k}_i were estimated to provide calipers for the extremal areas consistent with the corresponding experimental value.

(c) The energies $E(\mathbf{k}_i)$ were then calculated and the standard deviation of these energies from the average energy of all points was then minimized by variation of the $U_{\mathbf{g}}$'s and λ_p .

(d) Using the value of the average energy as the Fermi energy, i.e.,

$$E_F = -\frac{1}{n} \sum_{i=1}^n E(\mathbf{k}_i), \quad (n = \text{No. of points})$$

the extremal areas of the Fermi surface were then calculated using the parameters determined in (c).

TABLE III. Fourier coefficients of local pseudopotential (in Ry).

$U_{200} = -0.1018$	$U_{220} = +0.0146$
$U_{101} = -0.0739$	$U_{211} = +0.0427$
$E_F = 0.7697$	
$\lambda_p = 0.013$	

(e) In cases where the calculated value differed from the experimental one, the caliper points \mathbf{k}_i on that piece were relocated so as to bring the calculated area into agreement.

(f) Using the revised set of caliper points, steps (c)–(e) were then repeated until deviations of calculated from experimental areas were minimized.

The above procedure was carried out using the local form of the pseudopotential with the spin-orbit interaction included. These calculations were made using expansions of up to 22 plane waves for $\phi_{\mathbf{k}}$, the exact number being determined by conformity to the star-of- k group symmetry at the symmetry point in the immediate vicinity of the calculated points. These symmetry points and the corresponding size of the plane-wave sets are listed in Table II. With the inclusion of spin-orbit effects, the secular equation to be solved was of order 88.

Table III lists the final potential coefficients along with λ_p and E_F . It should be observed that in this calculation the *only* condition placed upon the potential coefficients and λ_p was that they give the best fit to the selected experimental data. Also, as a consequence of the fitting procedure, the Fermi energy is uniquely determined within our model and does not have the status of a variable parameter.

The final set of potential coefficients along with the determined value of λ_p were used to calculate the $E(\mathbf{k})$ bands. Shown in Fig. 5, these bands exhibit the expected removal of degeneracy due to spin-orbit effects along the XL and XP zone line, while maintaining a double degeneracy at X and L only. This group-theoretical consistency of the calculated band structure is automatically guaranteed by the selection of appropriate expansion sets for various symmetry points in the zone. Near W , where the spinless levels of zones 4, 5, and 6 are quite close together and where accidental degeneracies are found, the spin-orbit energy is comparable to the separation energy of the bands and spin-orbit effects are very pronounced. All accidental degeneracies are found to be lifted and the fifth and sixth bands are raised significantly in energy.

It has been noted that the spin-orbit parameter λ_p has been determined solely as a fitting parameter due to the lack of an accurate experimental determination of the strength of the interaction. It has been found, however, that the spin-orbit splittings for the valence electrons in a solid tend to approximate the corresponding atomic values. We would thus expect the low-lying p -like states at Γ to exhibit a spin-orbit splitting comparable to that of the singly ionized tin atom. The experimental value⁴² for this atomic case is 3.9×10^{-2} Ry. We find that our model predicts a corresponding spin-orbit splitting of 4.4×10^{-2} Ry. This agreement is quite reasonable considering that the relation between

⁴² Natl. Bur. Std. (U. S.) Circ. 467 (1949).

TABLE IV. Calculated and experimental extremal cross-sectional areas.

Symbol	Coordinates of \mathbf{H}		A_{calc}	A_{expt}	$10^{-3} \times \Delta E_F$	A_{Weisz}
	θ	φ				
δ_1^1	0°	...	4.60×10^{-3}	4.59×10^{-3}	+0.04	3.34×10^{-3}
δ_1^2	0°	...	8.72×10^{-3}	8.68×10^{-3}	+0.45	8.10×10^{-3}
ϵ_1^2	0°	...	9.20×10^{-2}	9.14×10^{-2}	-0.43	1.15×10^{-1}
ϵ_1^4	0°	...	2.78×10^{-1}	2.76×10^{-1}	+0.67	...
ϵ_1^5	0°	...	3.03×10^{-1}	3.00×10^{-1}	-2.10	3.19×10^{-1}
π_1^5	0°	...	1.44×10^{-1}	1.42×10^{-1}	+1.34	1.52×10^{-1}
π_1^6	0°	...	1.67×10^{-1}	1.69×10^{-1}	+1.30	...
π_1^7	0°	...	1.84×10^{-1}	1.82×10^{-1}	-1.22	2.17×10^{-2}
τ_1^1	0°	...	1.19×10^{-2}	1.19×10^{-2}	...	7.5×10^{-3}
δ_2^1	90°	0°	4.16×10^{-2}	4.25×10^{-2}	-1.25	...
ϵ_1^1	90°	0°	8.87×10^{-2}	8.85×10^{-2}	+1.54	8.41×10^{-2}
π_1^1	90°	0°	5.56×10^{-2}	5.52×10^{-2}	-0.27	7.37×10^{-2}
τ_1^1	90°	0°	1.22×10^{-2}	1.20×10^{-2}	-0.28	1.87×10^{-2}
δ_3^1	90°	45°	4.40×10^{-2}	4.50×10^{-2}	-1.21	3.61×10^{-2}
ϵ_3^1	90°	45°	6.84×10^{-2}	6.87×10^{-2}	-0.27	6.20×10^{-2}
π_2^3	90°	45°	1.82×10^{-1}	1.81×10^{-1}	-0.79	...
τ_3^1	90°	45°	1.54×10^{-2}	1.57×10^{-2}	+0.36	...

band sheets on the XP and XL zone lines in Fig. 7. Along XP the splitting is 4.8×10^{-3} Ry and along XL the splitting is 3.8×10^{-3} Ry. This corresponds to magnetic breakdown across the spin-orbit energy gap at fields of about 5 kG. Effects of magnetic breakdown across these relatively small energy gaps have been observed by several investigators. The area branches labeled A , B , and C in Fig. 4 are assigned to extremal areas on the Fermi surface corresponding to orbits formed by tunneling across the spin-orbit energy gaps between the fourth-zone hole sheet and the third-zone dumbbells. The combined third- and fourth-zone surfaces are shown in Fig. 8. The B and C breakdown orbits caused by tunneling at junctions 1 and 2 are also shown.

The completeness of the dHvA data enables us to use them to examine other aspects of our Fermi-surface model. The existence of the fourth-zone electron neck is verified by the simultaneous cutoff of three dHvA area branches at 70.5° from $[001]$. The experimental details of this cutoff are shown in Fig. 9(a). The three area branches ϵ_1^1 , ϵ_1^2 , and ϵ_1^6 are assigned to the extremal areas corresponding to the identically labeled electron orbits shown on the fourth-zone sheets in Figs. 3(b) and 3(c). Figure 9(b) demonstrates the quantitative relationship existing between the orbits associated with these extremal areas at the point of simultaneous cutoff. It is clear that at this point these branches must satisfy the condition $2\epsilon_1^1 + \epsilon_1^2 = \epsilon_1^6$. Experimentally, the area branches assigned to these

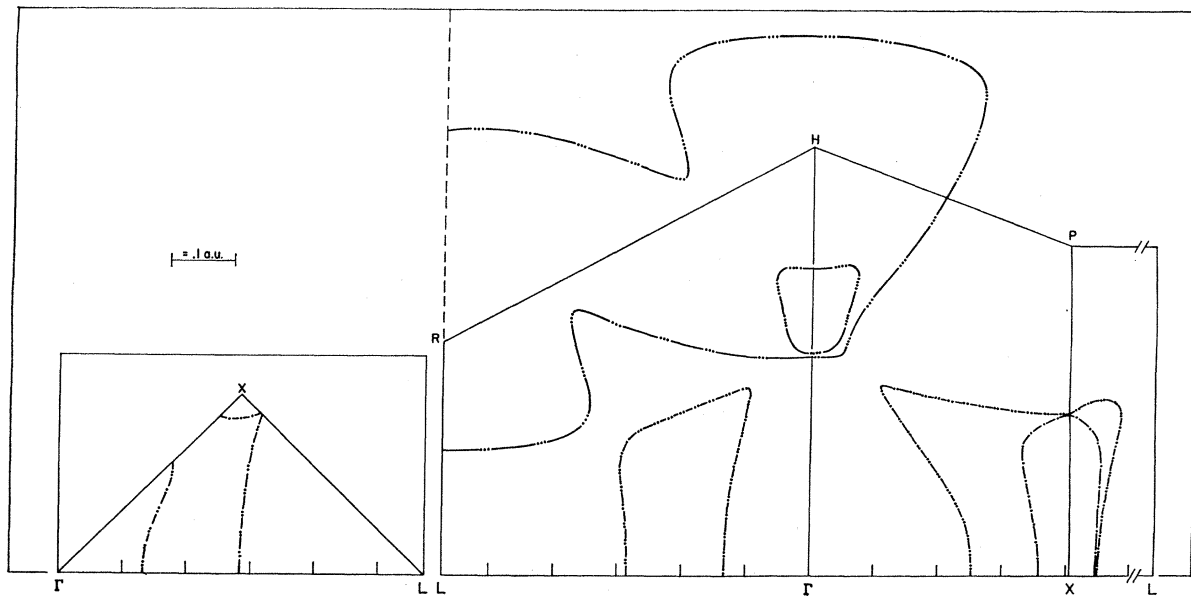


FIG. 7. Cross sections of the pseudopotential Fermi surface in the major crystallographic planes. The \cdot , \cdots , \cdots , and \cdots contours refer to the third, fourth, fifth, and sixth bands, respectively.

orbits agree very well with this quantitative relationship. Our calculated model predicts a cutoff angle of 71° for these branches, in very good agreement with the 70.5° observed experimentally.

Another cutoff angle observed in the dHvA data is that associated with the π_1^6 and π_1^7 area branches shown in Fig. 4. These branches are observed to experience a simultaneous merging and cutoff as \mathbf{H} is tilted from $[001]$ in the (100) plane. In Ref. 13 these branches were assigned to the maximal and minimal extremal areas on the fifth-zone pear surface shown identically labeled in Fig. 3(d). In Fig. 10 the relationship between these areas is shown for our model. Cross-sectional areas measured in planes perpendicular to \mathbf{H} are shown plotted as a function of position measured parallel to \mathbf{H} for three different values of θ . The angle θ_1 corresponds to an angle sufficiently small so that both maximal and minimal areas exist; θ_c is the critical angle at which these areas merge, and for angles greater than θ_c no extremal areas exist. Our model verifies the correctness of this relationship between the π_1^6 and π_1^7 extremal areas and the critical angle calculated from our model, $\theta_c = 15^\circ$, compared to the experimental value of 16° , further verifies the assignment made in Ref. 13.

In Ref. 13 there was one area branch, ϵ_1^3 , which could not be given a qualitative assignment to a corresponding sheet of Weisz's Fermi-surface model. On the basis of the present calculation, this area branch can be unambiguously assigned to the noncentral extremal orbit which traverses the outside of the fourth-zone hole sheet and the fourth-zone crossed lens electron sheet via the neck region joining them. The extremal areas calculated from our model for this orbit, as seen from the heavy dots on the ϵ_1^3 area branch in Fig. 4, are in very good agreement with the corresponding experimental values. With the assignment of

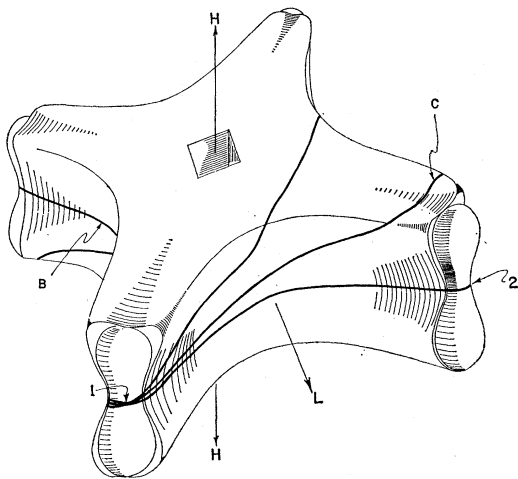


FIG. 8. The combined third- and fourth-zone Fermi surfaces. Magnetic breakdown generates the orbits across the spin-orbit energy gap.

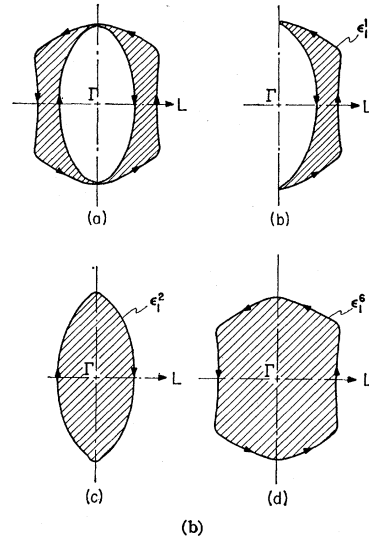
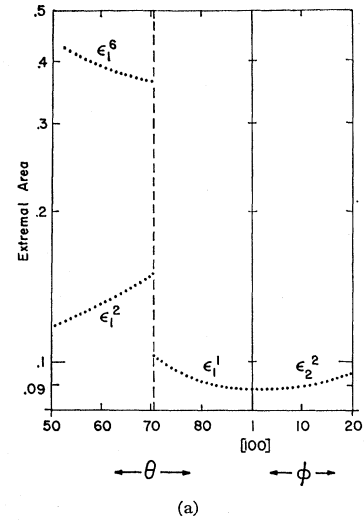


FIG. 9. (a) Three distinct area branches exhibiting an identical cutoff angle. All result from orbits in the fourth zone. (b) Individual orbits associated with the ϵ_1^1 , ϵ_1^2 , and ϵ_1^6 area branches. This schematic representation of the area branches shown in Fig. 9(a) demonstrates the quantitative relationship between those branches at the point of cutoff: $2\epsilon_1^1 + \epsilon_1^2 = \epsilon_1^6$.

the ϵ_1^3 area branch, all extremal area branches reported in Ref. 13 have been accounted for by assignment to corresponding extremal areas on sheets of our Fermi-surface model; furthermore, the calculated extremal areas for each of these assignments are shown to be in very good quantitative agreement with the experimental values.

The white-tin crystal structure is such that the Fermi sphere must accommodate exactly eight electrons. In this case the electrons are capable of filling exactly four zones and the volumes of electrons and holes are therefore equal. As a further check on the self-consistency of our model calculation, the number of electron and hole carriers in bands 3-6 were calcu-

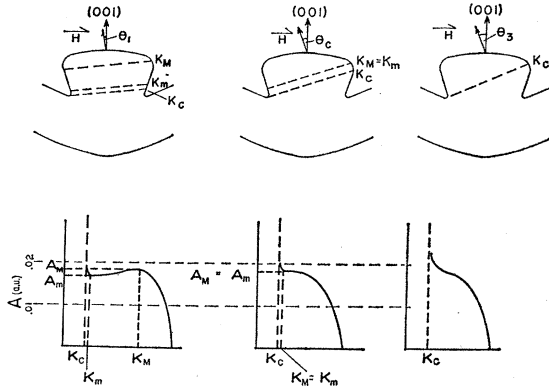


FIG. 10. Cross-sectional areas of the fifth-zone pear surfaces measured in planes perpendicular to \mathbf{H} as a function of position measured parallel to \mathbf{H} .

lated and found to be compensated to 2.7% of the total number of electron or hole states enclosed within the Fermi surface. This error is equivalent to a shift in Fermi energy of 1.0×10^{-3} Ry to attain exact compensation within our model.

Thus having established the consistency of this band-structure model with all of the dHvA data and also having demonstrated that it accounts, within calculational error, for all of the required electron states, we will now proceed to use it to reevaluate and reinterpret the results of several other experiments.

VII. OTHER EXPERIMENTS

A. rf Size Effect

The rf size-effect experiments of Gantmakher^{21,22} provide an excellent method for studying the geometry of the Fermi surface. By varying the magnetic-field direction, Gantmakher was able to measure calipers on many Fermi-surface sheets as a function of angle. This greatly facilitated the assignment of his extremal calipers to various sheets of our model. Cross corre-

lating Gantmakher's caliper branches with the dHvA area branches of Ref. 13 with respect to angular dependence, range, and relative size, we were able to assign unambiguously many of Gantmakher's experimental calipers to corresponding orbits on sheets of our Fermi surface model. Table V lists a comparison of the experimental semicalipers for the three major symmetry directions with those calculated from our model. Agreement is seen to be very good, the average difference being 2.5%. This is well below Gantmakher's estimated error of 8%. The agreement not only validates our assignment of experimental caliper branches, but also demonstrates the accuracy and completeness of Gantmakher's investigation.

This close agreement seems to belie our earlier observation of the quantitative disparity between the present calculation and that of Weisz. Since Weisz based his calculation on the experimental data of Gantmakher, it would be difficult to reconcile two models which agree in extremal calipers yet strongly differ in extremal areas. The solution to this apparent inconsistency is found in the fact that although, in most cases, Weisz's assignment of caliper branches to sheets of the Fermi surface was correct, calipers calculated from his model differed by as much as 30% from Gantmakher's value.

B. Magnetoresistance

Alekseevskii *et al.*¹⁸ have made a detailed study of the transverse magnetoresistance in tin. They found a continuum of open orbits existing for field directions lying in a solid angle around the [001] axis. This solid angle was determined only approximately and found to be limited to 35°–45° from [001]. They also found open orbits existing outside this range for all field directions in both the (100) and (110) planes, and for limited field directions in other planes of high symmetry.

From Fig. 3, we see that our model has two sheets capable of supporting open orbits: the fourth-band crossed-tube hole sheet in Fig. 3(c) and the fifth-band multiply connected tube network shown in Fig. 3(d).

The fifth-zone surface is capable of supporting aperiodic open orbits for all field directions for which the closed orbit π_1^5 , also shown in Fig. 3(d), exists. It was found in Ref. 13 that the extremal π_1^5 orbit was cut off at $\theta=35^\circ$ in the (100) plane. Anderson and Young,¹⁶ in their study of the magnetoresistance in tin were able to obtain more accurate measurements of the limits of the aperiodic open-orbit region than were obtained by Alekseevskii *et al.* They, in fact, were able to discriminate in some cases between open orbits on the fifth and fourth bands. Their limiting angle for the π_1^5 orbit in the (100) plane was found to be 38°. The value of 36° for this angle calculated from our model is in very good agreement with both of these empirical limits. Toward [110], our model shows this orbit limited to 25°. This agrees well with the limiting angle

TABLE V. Calculated and experimental extremal semicalipers.

Symbol	Coordinates of \mathbf{H}		Caliper direction	P_{calc}	P_{expt}
	θ	φ			
δ_1^1	0°	...	[100]	0.04	0.04
ϵ_1^2	0°	...	[100]	0.178	0.177
ϵ_1^5	0°	...	[100]	0.289	0.295
π_1^5	0°	...	[100]	0.200	0.197
π_1^7	0°	...	[100]	0.225	0.229
δ_2^1	0°	...	[110]	0.046	0.051
δ_2^2	0°	...	[110]	0.074	0.072
δ_2^3	0°	...	[110]	0.049	0.049
ϵ_1^2	0°	...	[110]	0.252	0.248
ϵ_1^5	0°	...	[110]	0.359	0.377
π_1^7	0°	...	[110]	0.268	0.267
ϵ_2^1	90°	45°	[001]	0.284	0.283
π_2^3	90°	45°	[001]	0.252	0.243
ϵ_1^1	90°	0°	[001]	0.303	0.293
π_1^1	90°	0°	[001]	0.150	0.146
τ_1^1	90°	0°	[001]	0.068	0.065

of 24° for the corresponding extremal area branch determined in Ref. 13.

The fourth-zone surface in Fig. 3(c) is also capable of supporting aperiodic open orbits for field directions near $[001]$. The ϵ_1^5 orbit shown in this figure is the orbit whose existence determines the existence of aperiodic open orbits on this surface. Our model limits this orbit to within 36° of $[001]$ in the (100) plane. This agrees well with the limiting angle of 35° for the ϵ_1^5 area branch of Ref. 13 and the 38° of Ref. 16. Toward $[110]$, our model gives a limiting angle of 42° . The corresponding area branch on Ref. 13 was only followed for 37° . This is probably due to the magnetic breakdown effects discussed earlier. In Ref. 16, a limiting angle of 44° was found for aperiodic open orbits in the (110) plane, in good agreement with our calculated value.

We have also calculated the limiting angles for the periodic open orbits which exist when the magnetic field is constrained to move in planes perpendicular to directions of high symmetry on the Fermi surface. The limiting angles for these directions are listed for both the fourth- and fifth-band sheets in Table VI along with the corresponding limiting angles determined experimentally in Ref. 18. Figure 11 shows a stereogram of the field directions for open orbits. Region I shows the experimental results from Ref. 18, while regions II, III, and IV are the directions calculated from our model for the combined fourth- and fifth-band surfaces, the fourth-band sheet, and the fifth-band sheet, respectively.

Since the fifth-band surface is oriented with the connecting tubes along $[100]$, a broad band of open orbits should exist for all field orientations in the (100) plane. The fourth-band tubes are oriented along the $[110]$ direction. According to our model, a broad band of open orbits will exist on this surface for field orientations in (110) up to 71° from $[001]$ after which a narrow band of open orbits will exist to within 2.5° of the $[110]$ axis. There are no open orbits on the fourth-zone sheet of the Fermi surface for magnetic fields in the $[110]$ direction. This contrasts with Weisz's calculation which predicts the existence of a narrow band of open orbits for this field orientation. Both models predict the existence of a narrow band of open orbits on the fifth-band sheet for fields oriented along $[110]$. Evidence for this narrow band of open electron trajectories has been reported in Ref. 16.

TABLE VI. Limiting angles for open orbits in particular symmetry planes.

Plane of \mathbf{H}	θ_{\max} (deg) 4th zone	θ_{\max} (deg) 5th zone	θ_{\max} (deg) expt
(150)	49	40	53
(130)	61	57	61
(120)	51	41	52
(230)	47	46	47

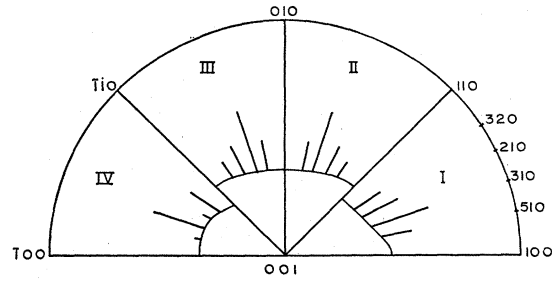


Fig. 11. Stereogram of the field directions for open orbits. Region I shows the experimental results from Ref. 18. Regions II, III, and IV are the field directions from this model for the combined fourth- and fifth-band sheets, the fourth-band sheet, and the fifth-band sheet, respectively.

C. Hall Effect

In the above discussion of open orbits, an important property of the tin Fermi surface was not considered. Tin has eight electrons per unit cell. These are capable of filling exactly four Brillouin zones so that when only closed orbits exist, compensation is to be expected. For the particular field direction $\mathbf{H} \parallel [001]$, however, even though only closed orbits are possible, the phenomenon of geometric discompensation occurs. The number of carriers is geometrically related to the Fermi-surface contours in the Brillouin zone by

$$n = \int dk_z \left(\oint_s dk_x dk_y \right), \quad (12)$$

where s is a closed contour on the Fermi surface in a plane perpendicular to the k_z axis. The direction of circulation determines the electron or hole character of the carriers. In the case of tin there are closed contours in the fourth and fifth zones formed by Bragg reflection at the zone boundaries. This results in the existence of electronlike orbits on the open fourth-zone hole sheet and holelike orbits on the open fifth-zone electron sheet, causing a disparity between the relative concentrations of electrons and holes. If the carrier trajectories are all closed, as is our case in white tin with \mathbf{H} along $[001]$, then the Hall "constant" R is a true constant determining the difference between electrons and holes. For the case of open trajectories, R becomes a complicated function having no simple physical meaning.

A detailed study of the Hall effect in white tin was made by Kachinskii.³ Consistent with our model prediction, he found that only when \mathbf{H} was parallel to $[001]$ did the Hall emf depend upon the magnetic field in a linear manner. The Hall coefficient in this case was found to be negative and corresponded to a concentration of 0.35 negative carriers per atom. From our model for this singular direction of the magnetic field, we calculate a negative concentration of 0.32 carriers per atom. This reasonable agreement supports the contention that the lack of compensation for this

particular field direction is due to closed orbits on our open fourth- and fifth-band sheets.

D. Cyclotron Resonance

A direct and accurate method of measuring the effective masses of conduction electrons is that involving the study of cyclotron resonance. Just as in the rf size-effect experiment, these cyclotron resonance investigations measure singularities in the surface impedance of a sample in an applied magnetic field and a time varying electric field applied parallel to the sample surface. When the applied frequency is the same as the natural cyclotron frequency of the electrons circling the Fermi surface in planes perpendicular to \mathbf{H} , the conductivity will exhibit a singularity. This resonance frequency ω_c is related to the effective mass of the electrons m^* by

$$m^* = eH/\omega_c c. \quad (13a)$$

The effective mass is also geometrically related to the Fermi surface by the relation

$$m^* = (1/\pi)\partial A/\partial E, \quad (13b)$$

where A is the area enclosed by the orbit in the plane normal to \mathbf{H} , and E is the energy at the Fermi surface. In practice, the effective masses measured by this experimental technique generally correspond to extremal orbits on the Fermi surface.

The cyclotron masses for extremal orbits on the Fermi surface of metallic tin have been studied extensively by Khaikin.²⁴ In his investigation, Khaikin was able to follow the angular dependence of these masses over long angular ranges in the major crystallographic planes. As with Gantmakher's semicaliper branches, the angular dependence of many of Khaikin's cyclotron mass branches allows them to be assigned unambiguously to corresponding sheets of our model Fermi surface by comparison with the dHvA area branches of Ref. 13. Table VII shows a comparison of Khaikin's experimental effective masses for \mathbf{H} along symmetry directions with the corresponding calculated value from our model.

On the average, the masses calculated from the model are 20% smaller than the experimental masses. This enhancement factor is also listed in Table VII as a

percentage deviation for each mass and is probably attributable to electron-electron⁴⁴ and electron-phonon⁴⁵ interactions.

VIII. CONCLUSION

The pseudopotential formalism, in conjunction with data from dHvA investigations, has been successfully applied to the generation of model band structures for several polyvalent metals. Its application to the construction of a model Hamiltonian or metallic tin, however, is particularly demanding. The complexity of the tin Fermi surface and the significance of the spin-orbit effects combine to challenge the accuracy of this model Hamiltonian band-structure representation and also test the validity of the assumptions made in its formulation. While the data used to generate the entire Fermi surface are limited to certain portions of the surface, the extent of the selected data used places strong restrictions on the generated model. These restrictions determine the relative positions of the energy bands in the immediate vicinity of the Fermi energy and, to the extent that the one-electron approximation is valid, allow us to generate the entire band structure.

The local pseudopotential calculation reported in this paper provides an accurate model for the tin Fermi surface. Not only does the model agree with the dHvA extremal areas used to generate it, as well as all other aspects of the dHvA data, but it has been shown to be quantitatively consistent with experiments which have examined other properties related to the Fermi surface. This consistency gives us confidence in the essential correctness of the model and justifies the application of the pseudopotential formalism in this specific case.

In contrast to the earlier semiempirical band-structure calculations for magnesium, zinc, and cadmium which employed pseudopotential techniques in conjunction with dHvA data, the purely local form of the pseudopotential was found to provide an adequate representation for the white-tin band-structure model. In the cases of the other three metals, the \mathbf{k} dependence of the pseudopotential was significant enough to necessitate the inclusion of the core terms in the model calculation.⁴⁶

ACKNOWLEDGMENTS

I would like to express my gratitude to Professor R. W. Stark for encouragement, patience, and guidance throughout all phases of this work.

⁴⁴ T. M. Rice, Ann. Phys. (N.Y.) **31**, 100 (1965).

⁴⁵ N. W. Ashcroft and J. W. Wilkins, Phys. Letters **14**, 285 (1965).

⁴⁶ As an aid to the quantitative application of our model for the interpretation and evaluation of investigations concerned with the Fermi surface of white tin, the coordinates of a network of points lying on the Fermi surface in each Brillouin zone are listed in Tables VIII-XI. For this supplementary material, order NAPS Documents from ASIS National Auxiliary Publications Service, % CCM Information Sciences, Inc., 22 West 34th Street, New York, New York 10001; available in microfilm or photocopies.

TABLE VII. Calculated and experimental effective masses.

Symbol	Direction of \mathbf{H}		m_{calo}^*	m_{expt}^*	$10^2 \times \Delta m/m_{\text{calo}}^*$
	θ	φ			
δ_1^1	0°	...	0.089	0.10	12.3
ϵ_1^2	0°	...	0.40	0.46	15.0
ϵ_1^5	0°	...	0.51	0.57	11.8
π_1^5	0°	...	0.49	0.64	30.6
π_1^7	0°	...	0.52	0.61	17.3
ϵ_1^1	90°	0°	0.41	0.53	29.3
π_1^1	90°	0°	0.47	0.50	6.4
τ_1^1	90°	0°	0.22	0.27	22.7
ϵ_3^1	90°	45°	0.35	0.41	17.1
π_2^3	90°	45°	0.61	0.78	27.8
τ_2^1	90°	45°	0.30	0.38	26.7